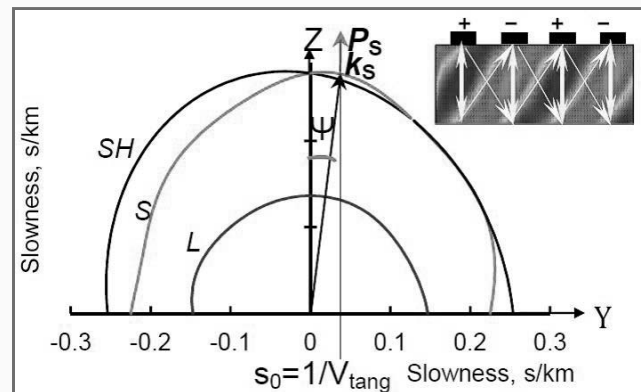


Spurious Modes in Laterally Excited Bulk Acoustic Resonators (XBARs): Analysis and Suppression

Natalya F. Naumenko[®], Member, IEEE

Abstract—Laterally excited bulk acoustic resonators (XBARs) are plate mode resonators in which one of the higher-order plate modes transforms into the bulk acoustic wave (BAW) due to the very thin plates used in these devices. The propagation of the primary mode is usually accompanied by numerous spurious modes, which deteriorate resonator performances and restrict potential XBARs' applications. This article suggests a combination of different methods for insight into the nature of the spurious modes and their suppression. Analysis of the BAW slowness surface provides optimization of XBARs for single-mode performance in the filter passband and around it. The rigorous simulation of admittance functions in the optimal structures allows for further optimization of electrode thickness and duty factor. Finally, the nature of different plate modes generated in a wide frequency range is clarified via simulation of dispersion curves, which characterize acoustic mode propagation in a thin plate under the periodic metal grating, and visualization of displacements accompanying wave propagation. Application of this analysis to lithium niobate (LN)-based XBARs demonstrated that in LN cuts with Euler angles (0° , 4° – 15° , 90°) and plate thickness dependent on orientation and varying between 0.05 and 0.1 wavelengths, the spurious-free response could be achieved. Due to tangential velocities of 18–37 km/s combined with the coupling of 15%–17% and feasible duty factor $a/p = 0.5$, the found XBAR structures can be applied in high-performance 3–6 GHz filters.



Index Terms—Lamb wave, laterally excited bulk acoustic resonator (XBAR), lithium niobate (LN), slowness surface, spurious modes.

I. INTRODUCTION

ACOUSTIC filters based on surface acoustic wave (SAW) or bulk acoustic wave (BAW) propagation in a piezoelectric medium are key elements of wireless communication systems. In the past decade, the explosive development of 5G technologies generated a strong demand for high-performance filters operating in front-end radio frequency (RF) bands. It led to an ongoing competition between SAW and BAW filter technologies [1].

SAW filters exhibit excellent selectivity, small size, and design flexibility supported by well-developed device fabrication technologies and advanced simulation tools.

Manuscript received 17 January 2023; accepted 7 March 2023. Date of publication 10 March 2023; date of current version 25 May 2023. This work was supported in part by the Russian Science Foundation under Grant 21-12-00247.

The author is with the Acousto-Optical Research Center, National University of Science and Technology MISIS, 119049 Moscow, Russia, and also with the Research Department, Moscow Technical University of Communications and Informatics, 111024 Moscow, Russia (e-mail: nnaumenko@ieee.org).

Digital Object Identifier 10.1109/TUFFC.2023.3255260

However, since the operating frequency of the SAW filter is proportional to SAW velocity and inversely proportional to the period of the electrode structure, it is limited by the maximum SAW velocity in a substrate and minimum linewidth achievable with standard optical photolithography. Hence, in conventional SAW filters, it does not exceed 2.5 GHz.

The available frequency range of SAW filters can be expanded to higher frequencies if a regular lithium niobate (LN) or lithium tantalate (LT) substrate commonly used in RF filters is replaced by a thin plate bonded to a high-velocity substrate [2], [3], [4], [5]. More options appear if LT or LN plate is combined with a strongly anisotropic substrate, e.g., quartz or langasite. Rotation of the substrate orientation enables lossless propagation of some modes with velocities of 5500–6500 m/s [6], [7], [8]. The electromechanical coupling k^2 of these high-velocity modes achieves 7% in LT/quartz, 18% in LN/quartz, and 14% in LN/langasite, rendering the layered structures suitable for application in high-frequency, high-performance SAW devices. In LN/sapphire structures, guided modes with coupling up to 5% can propagate even

Highlights

- **Method of optimization based on analysis of the slowness surface and providing the spurious-free performance of laterally excited bulk acoustic resonators (XBARs) is presented.**
- **In the analyzed orientations of LiNbO_3 , a higher-order plate mode A_1 can be efficiently transformed into the standing bulk wave with vertical Poynting vector, uncoupled with spurious modes.**
- **The found XBAR structures can be applied in high-performance 3–6 GHz filters due to tangential velocities of 18–37 km/s combined with the coupling of 15–17% and feasible duty factor $a/p = 0.5$.**

faster (9000–11 000 m/s) [9]. Thus, the application of layered SAW substrates allows for increased operating frequencies of SAW devices produced with standard optical lithography up to 4–6 GHz.

BAW technology has been adopted for commercial filters operating in the 3–7 GHz frequency range [10]. BAW filters offer lower losses and higher power handling capacity than SAW filters. However, the design and fabrication of a high-performance thin film bulk acoustic resonator (FBAR) or solidly mounted resonator (SMR) is a challenging and costly process, especially compared to low-cost SAW devices fit for mass production. AlN film, commonly used in BAW resonators as a piezoelectric layer, provides an electromechanical coupling of 4%–6% or lower, thus limiting the achievable width of the filter passband. Enhanced coupling required for wider bandwidths can be obtained with Sc-doped AlN films [11], but acoustic losses grow, and resonator performance degrades with increasing Sc content.

Like SAW devices, BAW devices received the new impulse from the latest technological achievements, such as *smart cut* technology, which incorporates ion implantation, wafer bonding, and thermal splitting [12]. It allows the fabrication of wideband BAW devices with ion-sliced single-crystalline LN layers of desired orientations. In SMR-type devices, acoustic mirror layers are arranged between the LN layer and a substrate. In FBAR structures, the cavity is arranged between the thin LN membrane and the primary substrate (e.g., Si). Some examples of SMR and FBAR devices based on ion-sliced LN layers have been reported [13], [14].

The advantages of SAW and BAW devices are combined in a plate mode resonator, where one of the higher-order modes is laterally excited by interdigital transducers (IDTs) located on a plate surface. The tangential velocity of the higher-order plate mode increases with decreasing plate thickness until this mode transforms into the vertically propagating BAW. Hence, at the specific plate thickness, SAW energy transforms into the standing BAW. Low propagation losses typical for guided modes can be combined with extremely high velocities required for high-frequency applications, while the variation of IDT parameters provides design flexibility.

In 2011, Kadota and Ogami [15] reported on a 5.4 GHz filter exploiting the first-order anti-symmetric A_1 mode propagating with velocity $V = 15\,200$ m/s and coupling $k^2 = 20\%$ in a thin ZX-LN plate of 400 nm thickness. In a very thin plate, multiple laterally excited spurious modes usually accompany the propagation of a high-velocity mode. Some of these modes can be suppressed with 90° rotation of the propagation direction on the Z-plane: in ZY-LN cut shear horizontally

polarized (SH) modes are uncoupled with the electric field generated by IDTs, due to crystal symmetry. Hence, only sagittally polarized modes (Lamb waves) are laterally excited in the ZY-LN plate.

Few research groups designed and investigated the plate mode resonators based on anti-symmetric Lamb wave A_1 propagating in the ZY-LN plate [16], [17], [18]. The submicrometer thickness (250–400 nm) of LN plates required for 3–6 GHz filters makes them fragile and restricts applications at higher frequencies. However, due to smart-cut technology, perfect high-quality suspended LN membranes of 400 nm or lower thickness can be produced. Hence, the transformation of A_1 mode into the vertically propagating shear BAW can be achieved. This plate mode resonator type, called laterally excited bulk acoustic resonators (XBARs) [16], was further investigated theoretically and experimentally [19], [20], [21].

Though XBAR looks attractive for high-frequency applications, some challenges should be addressed to make these devices suitable for mass production. In addition to the mechanical robustness of suspended thin LN films and power handling at high frequencies, these challenges include multiple spurious modes accompanying the propagation of the primary mode and deteriorating devices' performances [17], [18], [19]. Recently, the method of spurious mode suppression in XBARS, based on analysis of acoustic anisotropy of a piezoelectric material, was suggested [22], [23], and its efficiency was demonstrated for LN-based and LT-based XBARS.

This article suggests a comprehensive study of spurious modes using a combination of methods to clarify the nature of different modes and suppress them. The method of optimization based on analysis of the BAW slowness surface and its application to LN-based XBARS is described in Section II. The rigorous simulation of admittance functions in the found optimal structures allows for further optimization of electrode thicknesses and duty factors in XBARS. The nature of different plate modes generated in a wide frequency range is clarified in Section III via simulation of dispersion curves, which characterize acoustic mode propagation in a thin plate under the periodic metal grating, and visualization of displacements accompanying wave propagation.

II. XBAR OPTIMIZATION BASED ON ANALYSIS OF BAW SLOWNESS SURFACE

Fig. 1 shows a schematic view of XBAR as an example of a plate mode resonator. A thin plate (membrane) of a piezoelectric material with electrodes of IDT atop is mechanically supported by Si bases. The axes X_1 – X_3 shown in the figure are adjusted with the propagation direction X_1 of SAW generated

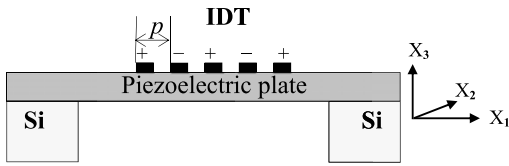


Fig. 1. Schematic of a plate mode resonator (or XBAR) and coordinate axes X_1 – X_3 used to specify the substrate orientate in SAW devices.

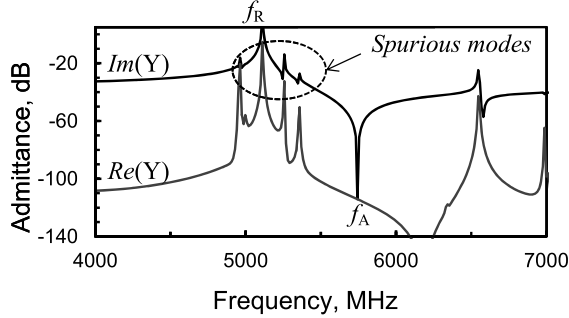


Fig. 2. Simulated admittance of the previously reported XBAR [20] based on ZY-LN with plate thickness $h = 380$ nm and Al electrode thickness $h = 100$ nm. The spurious modes observed between resonance (f_R) and anti-resonance (f_A) agree with the measured XBAR characteristics.

on the plate surface $X_3 = 0$. The orientation of these rotated axes with respect to the crystal axes is defined by the Euler angles (φ , θ , ψ), commonly used to specify the orientation of a substrate in SAW devices.

XBARS combine certain features of SAW and BAW resonators. Like in the BAW resonator, the resonant frequency of XBAR depends on the bulk wave velocity along the X_3 axis and plate thickness. However, the total spectrum of laterally excited acoustic modes depends strongly on the periodicity of the electrode structure along the X_1 axis in IDTs and metal gratings used to generate SAW and transform it into BAW.

Fig. 2 demonstrates an example of a simulated admittance function. It was obtained using the software SDA-FEM-SDA [24] for the previously reported XBAR structure [20] based on a ZY-LN plate of 380 nm thickness, with Al electrodes of 100 nm thickness, IDT period $p = 3$ μm , and duty factor $a/p = 0.166$ defined as the ratio of the IDT electrode width a to the electrode period p . The simulated function agrees with the reported experimental response and reveals that several spurious modes are laterally excited in the frequency range between resonant (f_R) and anti-resonant (f_A) frequencies and around it. These modes appear as multiple combinations of acoustic waves generated by IDTs and satisfying boundary conditions in the analyzed structure.

A higher-order plate mode (e.g., Lamb wave) generally comprises tilted BAWs propagating along the plate and being reflected at its top and bottom surfaces. With decreasing plate thickness, one of the tilted BAWs transforms into the vertically propagating bulk wave. The *critical* plate thickness, which ensures the transformation of tilted BAWs into the standing bulk wave along the X_3 axis, can be considered a numerical criterion of a *true* XBAR. Such a device can be identified as a particular type of plate mode resonator. The critical plate thickness depends on the orientation of a piezoelectric plate and can be determined from analysis of the BAW slowness surface, as described hereafter.

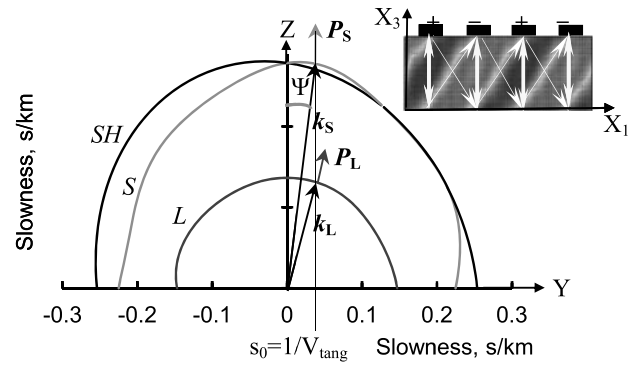


Fig. 3. Cross section of the BAW slowness surface by YZ plane of LiNbO_3 . The wave vectors \mathbf{k}_S and \mathbf{k}_L and Poynting vectors \mathbf{P}_S and \mathbf{P}_L refer to BAW modes contributing to the Lamb wave structure. The inset explains schematically wave propagation at *critical* frequency $f_0 = (2ps_0)^{-1}$ when the slow shear BAW has a tilted wave vector and vertical Poynting vector.

Fig. 3 shows the cross section of the BAW slowness surface by the YZ plane, which is the reflection symmetry plane of LN. This plane is sagittal for all orientations described by the Euler angles (0° , θ , 90°), i.e., when the plate cut is normal to $Z + \theta$ direction, and IDT electrodes generate a periodic electric field along the $Y + \theta$ direction. SH-BAWs propagating in the YZ plane and polarized along the X -axis are uncoupled with the electric field. In contrast, the longitudinal L-BAWs and shear S-BAWs polarized in the YZ plane are generated by IDTs. Different combinations of these BAWs compose sagittally polarized plate modes (Lamb waves).

The wave structure depends on frequency f , which can be converted into the slowness $s = (2pf)^{-1}$ or tangential velocity $V_{\text{tang}} = 1/s$ along the X_1 axis. S-BAW and L-BAW with wave vectors \mathbf{k}_S and \mathbf{k}_L and Poynting vectors \mathbf{P}_S and \mathbf{P}_L , respectively, are generally involved in the wave structure of a higher-order plate mode. The power flow angle Ψ between the \mathbf{k} and \mathbf{P} vectors depends on acoustic anisotropy and achieves 14.5° for shear BAWs propagating in the YZ plane of LN. Maximum anisotropy occurs in orientations close to the *acoustic axes* of a crystal. The intersection between S-BAW and SH-BAW sheets of the slowness surface and conical points on this surface characterize these specific directions. In LN and other crystals referred to the symmetry classes 3, $3m$ and 32 , one of the acoustic axes is parallel to the Z -axis of the crystal, and strong acoustic anisotropy occurs around it [25].

It enables the efficient transformation of SAW energy into the vertically propagating BAW. At the specific slowness $s = s_0$ (see Fig. 3), the Poynting vector \mathbf{P}_S of S-BAW becomes parallel to the Z -axis of a crystal. However, the wave vector \mathbf{k}_S remains tilted and has a nonzero tangential component. Such BAW can be efficiently reflected between a plate's top and bottom surfaces if the plate thickness h_{LN} satisfies the following condition: $h_{\text{LN}}/\lambda = \text{tg}(\Psi)/2$, where $\lambda = 2p$. The propagation of BAW with a tilted \mathbf{k} vector and vertical \mathbf{P} vector in a thin plate is explained schematically in the inset of Fig. 3. In this case, negligible coupling of the primary BAW mode with spurious modes can be expected.

In addition to low spurious modes, a high electromechanical coupling coefficient of the primary mode is desirable in XBARS. This parameter can be roughly estimated as

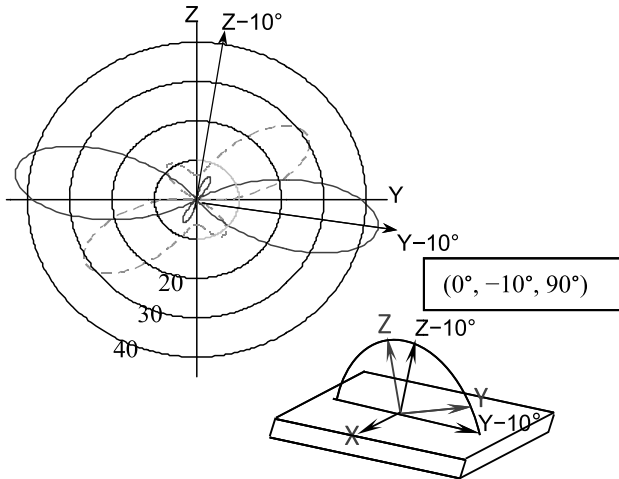


Fig. 4. Polar diagram of electromechanical coupling of longitudinal (dashed line) and shear (solid line) BAWs propagating in YZ plane of LN; orientation with Euler angles $(0^\circ, -10^\circ, 90^\circ)$ providing maximum coupling of the shear BAW.

$k_{\text{eff}}^2 = 2(V_p - V_n)/V_n$, where V_p and V_n are BAW velocities calculated with the piezoelectric effect and without it, respectively. Fig. 4 shows the polar diagrams of the coupling k_{eff}^2 obtained for longitudinal and shear BAWs propagating in the YZ plane of LN.

Lateral excitation of a plate mode is provided due to the electric field generated by IDTs. The electromechanical coupling of such a mode is determined by the shift of effective tangential velocity with switching between SC (resonance) and OC (anti-resonance) electric boundary conditions in the grating. This shift is proportional to the velocity difference $(V_p - V_n)$, or k_{eff}^2 estimated for BAWs traveling along the X_1 axis of a substrate. Fig. 4 demonstrates that maximum k_{eff}^2 is expected for shear BAWs propagating along the $Y - 10^\circ$ direction of LN when the plate surface is normal to the $Z - 10^\circ$ direction. The actual coupling of a plate mode is usually lower than the estimated k_{eff}^2 , but it vanishes if $k_{\text{eff}}^2 = 0$.

The orientation $(0^\circ, -10^\circ, 90^\circ)$, in which the shear BAW exhibits maximum coupling is shown in the inset of Fig. 4. LN orientations close to $(0^\circ, 33^\circ, 90^\circ)$ -cut enable high coupling of the longitudinal BAW. Therefore, layered structures combining these plates with high-velocity substrates were previously optimized for high-frequency wideband SAW devices [7], [8].

XBAR optimization procedure based on the analysis of the slowness surface consists of the following steps:

- 1) First, the slowness s_0 characterized by the vertical Poynting vector and the corresponding tangential velocity $V_{\text{tang}} = 1/s_0$ are estimated from the slowness surface.
- 2) Next, the power flow angle Ψ is determined as the angle between \mathbf{k}_s and \mathbf{P}_s at $s = s_0$.
- 3) Finally, the optimal plate thickness $h_{\text{opt}}/2p = \text{tg}(\Psi)/2$ is found.

This procedure was applied to LN orientations with Euler angles $(0^\circ, \theta, 90^\circ)$ and θ varying between -15° and $+20^\circ$. The high piezoelectric coupling of the shear BAW is combined here with sufficiently strong acoustic anisotropy. Fig. 5(a) shows the optimization results: the tangential velocity V_{tang} and the

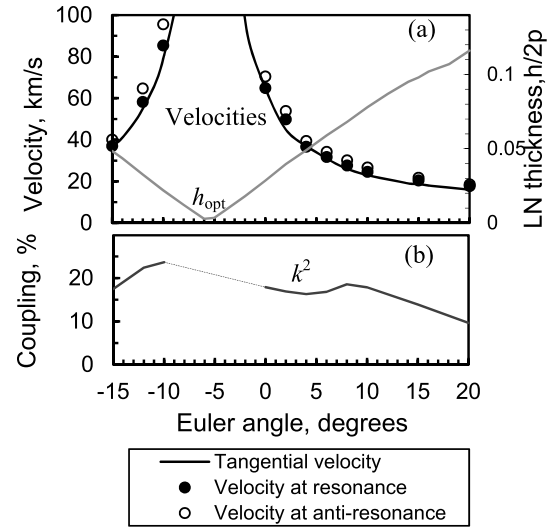


Fig. 5. Wave characteristics in $(0^\circ, \theta, 90^\circ)$ -LN plates with optimal plate thicknesses, as functions of the Euler angle θ . (a) Optimal LN thickness h_{opt} , tangential BAW velocities estimated from analysis of the slowness surface, and effective velocities extracted from admittance functions. (b) Electromechanical coupling.

optimal thickness h_{opt} are plotted as functions of the cut angle θ . The found XBAR structures with optimized plate thicknesses were verified further by rigorous simulation of the admittance functions of resonators based on these structures. The resonant (f_R) and anti-resonant (f_A) frequencies were extracted and converted into effective tangential velocities $V_R = 2pf_R$ and $V_A = 2pf_A$ [black and white circles in Fig. 5(a)]. Excellent agreement between the velocity dependencies $V_{\text{tang}}(\theta)$ and $V_R, V_A(\theta)$ in the analyzed orientations confirms the nature of observed modes as shear BAWs with vertical Poynting vectors. Fig. 5(b) shows the electromechanical coupling k^2 estimated from the difference between f_R and f_A .

The optimization procedure described above was previously applied to XBARs on LT plates [22], and the dependence $V_{\text{tang}}(\theta)$ obtained for this crystal also demonstrated excellent agreement with $V_R, V_A(\theta)$ extracted from the admittance functions. The method can be applied to any piezoelectric material if the normal to a plate X_3 and tangential axis X_1 belong to the reflection symmetry plane. Otherwise, laterally excited modes are composed of three BAWs instead of two. As a result, the number of spurious modes grows, and the coupling between them perturbs the resonator performance by multiple ripples. For example, in resonators based on the A_1 mode propagating in 128° -YX LN, exceptionally high electromechanical coupling can be achieved, but multiple spurious modes usually perturb the resonator performance [26]. Suppression of these modes requires laborious optimization via variation of plate and electrode thicknesses and duty factor or modified fabrication process, as suggested in [17].

In LN, the power flow angle estimated at the slowness s_0 tends to zero at $\theta \approx -6^\circ$, as well as the optimal plate thickness [see Fig. 5(a)]. As a result, V_{tang} grows dramatically and demonstrates extreme sensitivity to a minor variation in plate thickness. Hence, the trade-off between a high tangential velocity desirable for high-frequency devices and a minimum

plate thickness suitable for device fabrication is a significant challenge in selecting orientations for XBARS. For example, the power flow angles confined between 6° and 12° enable the optimal plate thicknesses between 0.05λ and 0.1λ , that is, between 300 and 600 nm if $\lambda = 2p = 6 \mu\text{m}$. This condition is satisfied in LN orientations with cut angles between $\theta = 4^\circ$ and $\theta = 15^\circ$ and the tangential velocity varying between 18 and 37 km/s. As a result, 3–6 GHz operating frequencies can be achieved in XBARS with $p = 3 \mu\text{m}$. The coupling of the primary mode varies between 14.3% and 16% in these LN orientations.

It should be mentioned that in the ZY cut, described by the Euler angles $(0^\circ, 0^\circ, 90^\circ)$, the optimal plate thickness is $h_{\text{opt}} = 0.028\lambda$. At least twice thicker plates were used in the previously reported experimental XBAR structures based on ZY-LN (e.g., $h_{\text{LN}} = 0.063\lambda$ [20]). A significant deviation of the plate thickness from the optimal value results in coupling between the primary mode and spurious modes and ripples in the XBAR response. Variations of duty factor and electrode thickness do not help suppress these spurious modes.

At least twice the larger IDT period should be used to achieve the optimal normalized thickness $h/2p$ providing the spurious-free response. However, a primary mode's resonant frequency and coupling will change because the tangential velocity is not a linear function of the IDT period. The resonator length grows with an increasing period, but the effective length depends also on the reflection coefficient in a periodic grating.

If the plate thickness is optimized using the method described above, the XBAR response remains spurious-free with a variation of duty factor in a wide range between 0.3 and 0.6. Hence, low duty factors $a/p = 0.15$ – 0.25 previously recommended to suppress the spurious modes [18], [19], [20] are unnecessary in XBARS with optimized plate thickness. A more feasible value $a/p = 0.5$ facilitates the fabrication of electrode structures in high-frequency resonators.

Three examples of simulated XBAR admittances obtained for LN orientations $(0^\circ, 0^\circ, 90^\circ)$, $(0^\circ, 5^\circ, 90^\circ)$, and $(0^\circ, 10^\circ, 90^\circ)$ with optimal plate thicknesses 0.028λ , 0.053λ and 0.078λ , respectively, are presented in Fig. 6(a)–(c). The electrode thickness $h_{\text{Al}} = 0.01\lambda$ and duty factor $a/p = 0.5$ were used in all structures. The admittances are shown as functions of the normalized frequency f/f_{R} , where f_{R} decreases from 10.83 GHz in $(0^\circ, 0^\circ, 90^\circ)$ -LN to 4.12 GHz in $(0^\circ, 10^\circ, 90^\circ)$ -LN if $p = 3 \mu\text{m}$. The coupling coefficient is nearly equal in three structures, $k^2 = 17.8\%$, and all responses are spurious-free in the range between f_{R} and f_{A} . Spurious-free responses can also be obtained in XBARS based on $(0^\circ, 15^\circ, 90^\circ)$ -LN of thickness $h_{\text{LN}} = 0.098\lambda$ and $(0^\circ, 20^\circ, 90^\circ)$ -LN of thickness $h_{\text{LN}} = 0.116\lambda$ [23] but these structures provide lower effective velocities (18–21 km/s) and lower coupling (10%–13%).

Fig. 6 reveals the presence of a ripple below resonance in all analyzed LN orientations. XBAR structure based on $(0^\circ, 10^\circ, 90^\circ)$ -LN was further investigated to clarify the nature of this ripple. The effective velocities of the primary mode (V_{R} , V_{A}) and the nearest spurious mode (V_{SPUR}) were estimated for XBARS with the plate thickness $h_{\text{LN}} = 0.078\lambda$

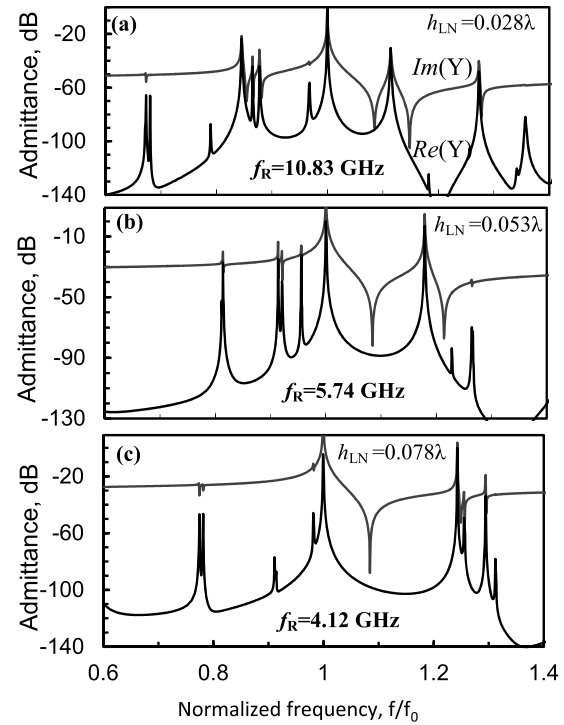


Fig. 6. Simulated admittances of XBARS based on different LN plates with optimal plate thicknesses. Al electrode thickness is 0.01λ . Duty factor is $a/p = 0.5$. (a) $(0^\circ, 0^\circ, 90^\circ)$ -LN. (b) $(0^\circ, 5^\circ, 90^\circ)$ -LN. (c) $(0^\circ, 10^\circ, 90^\circ)$ -LN.

as functions of duty factor or electrode thickness. Fig. 7(a) shows variations of V_{R} , V_{A} , and V_{SPUR} in the structures with $a/p = 0.1$ – 0.65 and fixed Al electrode thickness, $h_{\text{Al}} = 0.01\lambda$. The results of simulations for the structures with variable Al electrode thickness, $h_{\text{Al}} = (0.001$ – $0.03)\lambda$, and fixed duty factor $a/p = 0.5$ are shown in Fig. 7(b). In addition, the coupling k^2 of the primary mode was estimated.

When $a/p = 0.5$ and $h_{\text{Al}} = 0.01\lambda$, the analyzed spurious mode propagates at $f = 0.98f_{\text{R}}$. With decreasing a/p or h_{Al} , this mode shifts to higher frequencies and enters the interval (V_{R} , V_{A}) at $a/p < 0.34$ [see Fig. 7(a)] or at $h_{\text{Al}} < 0.007\lambda$ [see Fig. 7(b)]. Thus the structures with wider or thicker electrodes ensure better suppression of spurious modes, but the electromechanical coupling decreases with electrode thickness.

XBAR structure with duty factor $a/p = 0.5$ and Al electrode thickness 0.015λ were selected for further spurious modes' analysis because it combines high effective velocity of the primary mode ($V_{\text{R}} = 24.5$ km/s) with sufficiently high coupling ($k^2 = 17.2\%$). Fig. 8 demonstrates the effect of plate thickness variation on the characteristics of this XBAR structure. The effective velocities of the primary mode and several spurious modes are shown as functions of the plate thickness, which varies between $h_{\text{LN}} = 0.06\lambda$ and $h_{\text{LN}} = 0.09\lambda$. The primary mode propagates with velocities $V_{3\text{R}}$ and $V_{3\text{A}}$ strongly dependent on the plate thickness. One of the spurious modes exhibits velocity-versus-thickness dependence $V_2(h_{\text{LN}})$ nearly parallel to $V_{3\text{R}}(h_{\text{LN}})$ and $V_{3\text{A}}(h_{\text{LN}})$, while other spurious modes (V_1 , V_4 , V_5) show weaker dependence on the plate thickness. The best separation of the primary mode from the nearest spurious modes can be achieved when $h_{\text{LN}} \approx 0.075\lambda$, which

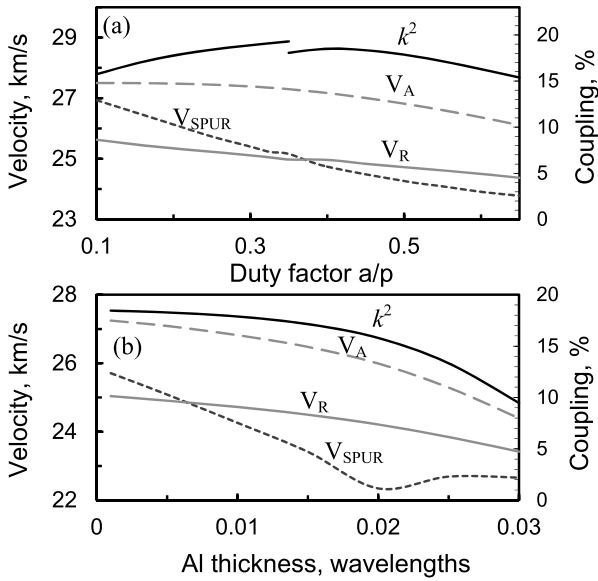


Fig. 7. Effective velocities (V_R , V_A) and electromechanical coupling (k^2) of the primary mode, and spurious mode velocity (V_{SPUR}) extracted from admittance functions of XBARs based on $(0^\circ, 10^\circ, 90^\circ)$ -LN: as functions of (a) duty factor at fixed electrode thickness $h_{Al} = 0.01\lambda$ and (b) Al thickness at $a/p = 0.5$. LN thickness is $h_{LN} = 0.078\lambda$.

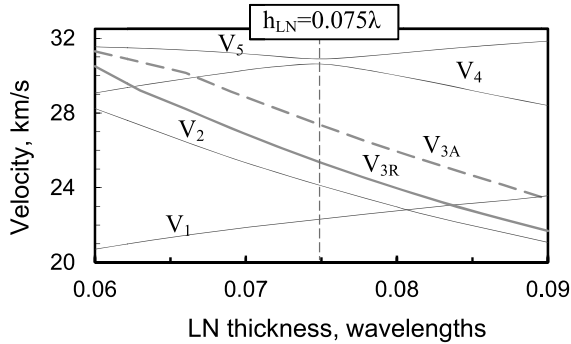


Fig. 8. Effective velocities of the main (V_{R3} , V_{A3}) and few spurious (V_1 , V_2 , V_4 , V_5) modes in XBARs based on $(0^\circ, 10^\circ, 90^\circ)$ -LN plate, as functions of LN thickness. Al thickness is $h_{Al} = 0.015\lambda$. Duty factor is at $a/p = 0.5$.

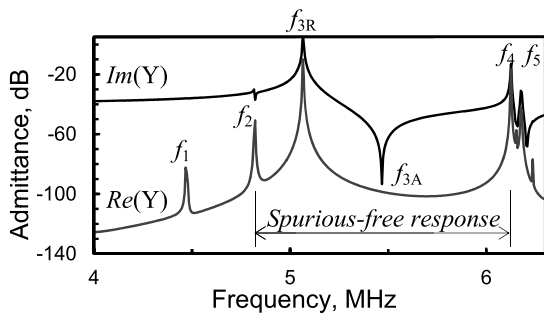


Fig. 9. Simulated admittance of XBAR structure on $(0^\circ, 10^\circ, 90^\circ)$ -LN providing the best suppression of the nearest spurious modes: LN thickness $h_{LN} = 375$ nm, IDT period $p = 2.5$ μ m, duty factor $a/p = 0.5$, and electrode thickness $h_{Al} = 75$ nm.

is close to the optimal thickness obtained from analysis of the slowness surface ($h_{LN} = 0.078\lambda$).

Fig. 9 shows the simulated admittance of XBAR based on $(0^\circ, 10^\circ, 90^\circ)$ -LN with plate thickness $h_{LN} = 0.075\lambda$. The IDT period $p = 2.5$ μ m yields the plate thickness $h_{LN} = 375$ nm, the electrode thickness $h_{Al} = 75$ nm, and the resonator frequencies $f_R = 5.06$ GHz, $f_A = 5.47$ GHz. As expected,

the response is spurious-free in a wide range between 4.85 and 6.2 GHz. The weak ripple at $f = 4.85$ GHz can be related to the lower-frequency edge of the stopband built by the primary mode. This assumption is further verified (see Section III) by rigorous simulation of dispersion caused by wave reflections from the top and bottom of a thin plate and electrodes of a periodic metal grating.

The optimal plate thickness enabling low spurious modes does not change significantly with a variation of electrode thickness within the interval $(0.01-0.03)\lambda$. However, if much thicker electrodes are required, for example, to decrease resistive losses, further optimization based on rigorous simulation of admittance functions is desirable. Orientations characterized by higher tangential velocities, such as $(0^\circ, -2^\circ, 90^\circ)$ -LN, are preferred for application in 5 GHz resonators with thick electrodes.

III. ACOUSTIC WAVE DISPERSION IN XBAR

Propagation of acoustic waves in a thin piezoelectric plate under the periodic metal grating induces the 2-D distribution of mechanical displacements in the X_1X_3 plane. The 2-D pattern is built by multiple reflections from electrodes of a periodic grating and wave reflections between the plate's top and bottom. The standing waves vibrating in XBAR are characterized by the wavelengths $\lambda_1 = 2p/n_1$ along the X_1 axis, where $n_1 = 1, 3, 5, \dots$, and $\lambda_3 = n_3(h_{LN}/2)$ along the X_3 axis, where $n_3 = 0$ for zero-order plate modes, $n_3 = 1, 3, 5, \dots$, for anti-symmetric modes, and $n_3 = 2, 4, 6, \dots$, for symmetric plate modes.

A rigorous solution of the boundary problem at the wavelength $\lambda_0 = 2p$ yields the spectrum of acoustic waves laterally excited by infinitely long IDTs. Fig. 10(a) shows the admittance function of XBAR based on $(0^\circ, 10^\circ, 90^\circ)$ -LN plate with optimal geometrical parameters determined in Section II.

The nature of each mode observed in Fig. 10(a) can be understood from the dispersion plot shown in Fig. 10(b). It was obtained by scanning the normalized tangential wavenumber $r = k/2k_0 = p/\lambda$ in a wide range between $r = 0$ and $r = 0.5$ ($\lambda_0 = 2p$). The admittance function was simulated at each normalized wavenumber, and resonant frequencies f_R of all observed modes were extracted. The obtained dependence of the normalized wavenumber $k/2k_0$ on frequency f represents the dispersion behavior $k(\omega)$ of acoustic waves in the analyzed XBAR structure. Each mode observed in Fig. 10(a) can be associated with two dispersion curves arising from $r = 0.5$. The distance between these curves at $r = 0.5$ determines the reflection coefficient of the analyzed mode in the periodic grating.

All modes can be divided into groups with similar dispersion behavior. The first group combines zero-order anti-symmetric Lamb wave $A_{0/1}$ and its harmonics $A_{0/3}$, $A_{0/5}$, $A_{0/7}$, and $A_{0/9}$ characterized by $n_3 = 0$ and $n_1 = 3, 5, 7$, and 9 . These modes can be observed in Fig. 10(a) at frequencies 0.16, 1.25, 2.81, 4.47, and 6.15 GHz. The displacement accompanying wave propagation, u_1 along the X_1 axis and u_3 along the X_3 axis, illustrate the structure of each mode (see Fig. 11). Zero-order anti-symmetric modes are characterized by $u_1 \approx 0$

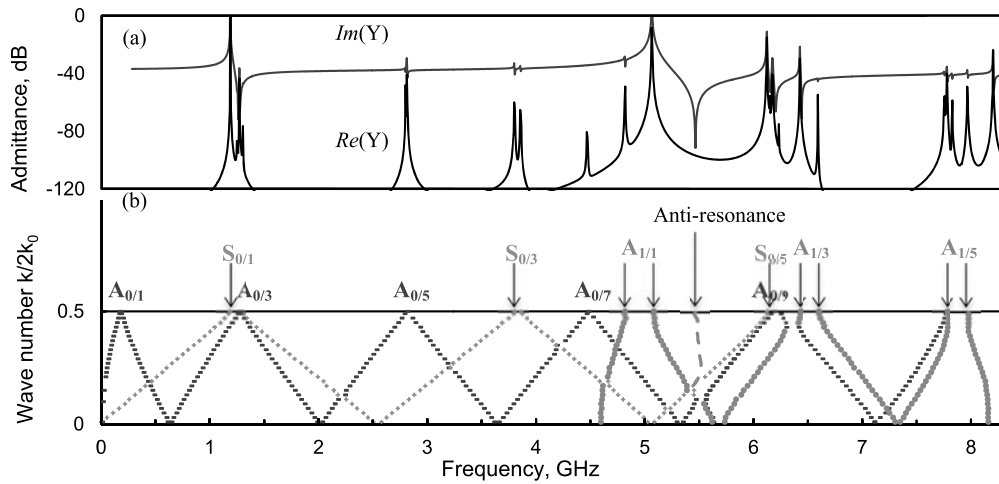


Fig. 10. (a) Admittance of XBAR based on $(0^\circ, 10^\circ, 90^\circ)$ -LN plate of optimal thickness. (b) Dispersion of plate modes propagation under periodic grating.

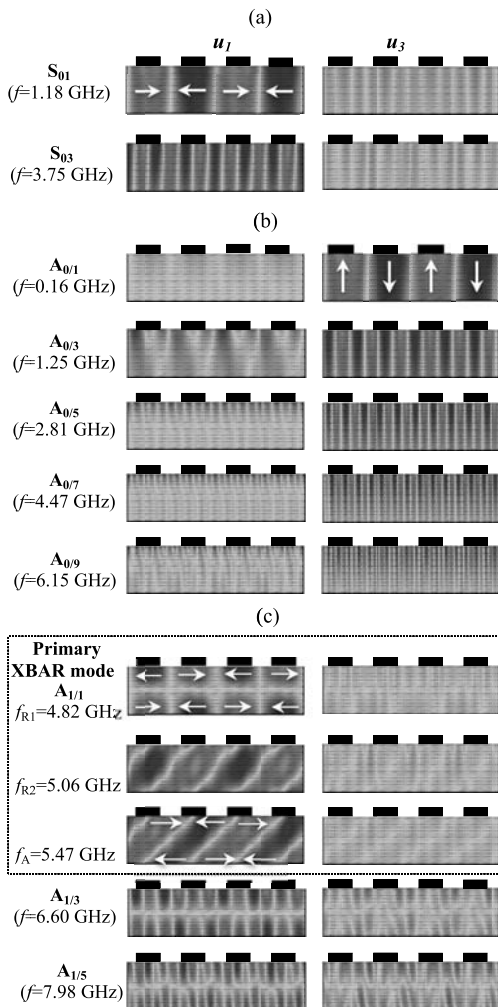


Fig. 11. Distribution of displacement components u_1 and u_3 in the sagittal plane $X_1 X_3$ illustrating the structure of symmetric and anti-symmetric plate modes propagating at different frequencies in XBAR using $(0^\circ, 10^\circ, 90^\circ)$ -LN. (a) Zero-order symmetric modes. (b) Zero-order anti-symmetric modes. (c) First-order anti-symmetric modes.

and homogeneous distribution of u_3 along the depth, with the same sign of u_3 at the top and bottom plate surfaces.

The second group combines zero-order symmetric modes $S_{0/1}$, $S_{0/3}$, and $S_{0/5}$ excited at frequencies 1.18, 3.75, and 6.15 GHz and characterized by $u_3 \approx 0$ and homogeneous distribution of u_1 along the depth. The perfect structure of the Lamb wave is perturbed when two different modes propagate with almost the same velocity. For example, at $f \approx 1.25$ GHz, the modes $S_{0/1}$ and $A_{0/3}$ interact. The interaction manifests itself by ripples of admittance function and nonzero displacement u_1 accompanying propagation of the mode $A_{0/3}$.

The third group of plate modes appears at $f > 4.85$ GHz and refers to the first-order anti-symmetric Lamb wave A_1 . The mode $A_{1/1}$ determines resonance at 5.06 GHz and anti-resonance at 5.47 GHz. They refer to the primary XBAR's mode with the largest k^2 . From the dispersion curve, it is clear that a weak spurious at 4.82 GHz occurs at the lower edge of the stopband built by reflections of the mode $A_{1/1}$ in a periodic metal grating. The opposite signs of u_1 at the top and bottom of the plate and negligible u_3 characterize this mode.

Analysis of the structure of $A_{1/1}$ at three different frequencies reveals wave transformation from BAW with a tilted wave vector and almost vertical Poynting vector (at $f_A = 5.47$ GHz) into the perfect Lamb wave (at $f_{R1} = 4.82$ GHz and $f_{R2} = 5.06$ GHz) when the plate thickness crosses the critical value.

With increasing frequency, a denser spectrum of acoustic modes results in coupling between the modes and perturbation of their structure. For example, the third harmonic of the first-order anti-symmetric plate mode, $A_{1/3}$, excited at 6.60 GHz, is perturbed by interactions with the modes $A_{0/9}$ and $S_{0/5}$.

The structure of the mode $A_{1/5}$ excited at 7.98 GHz looks even more complicated because of interactions between several modes. In addition to the wave structure's perturbation, the generation of numerous spurious modes can be observed.

IV. CONCLUSION

Multiple spurious modes accompanying propagation of the primary mode in XBARS and deteriorating XBAR performances can be efficiently suppressed if orientation and plate thickness are optimized based on analysis of the BAW

slowness surface. Optimization provides transformation of the first-order anti-symmetric Lamb wave A_1 into the standing shear BAW, which is strongly reflected between the plate's top and bottom surfaces and exhibits negligible coupling with the spurious modes. The required transformation of the wave nature can be achieved in crystal orientations with sufficiently strong acoustic anisotropy. The optimal plate thickness depends on orientation.

In the optimized structures, XBAR response remains spurious-free with a variation of duty factor in a wide range. It makes it unnecessary to use low-duty factors, previously recommended to suppress the spurious modes. A more feasible duty factor $alp = 0.5$ facilitates the fabrication of electrode structures for high-frequency resonators.

To summarize, the main advantage of the method based on analysis of the slowness surface is that it is fast and easy. In addition to the spurious-free response, the method fairly accurately predicts the frequency (tangential velocity) of the primary mode in the optimal structure, e.g., A_1 mode transformed into the shear BAW. Moreover, the application of the same method to the longitudinal BAWs propagating in the YZ plane enables optimization of the plate thickness for spurious-free response around the symmetric S_1 mode and estimation of its tangential velocity.

REFERENCES

- [1] A. Hagelauer et al., "From microwave acoustic filters to millimeter-wave operation and new applications," *IEEE J. Microw.*, vol. 3, no. 1, pp. 484–508, Jan. 2023, doi: 10.1109/JMW.2022.3226415.
- [2] M. Kadota and S. Tanaka, "Solidly mounted ladder filter using shear horizontal wave in LiNbO_3 ," in *Proc. IEEE Int. Ultrason. Symp. (IUS)*, Tours, France, Sep. 2016, pp. 1–4.
- [3] T. Takai et al., "High-performance SAW resonator on new multilayered substrate using LiTaO_3 crystal," *IEEE Trans. Ultrason., Ferroelectr., Freq. Control*, vol. 64, no. 9, pp. 1382–1389, Sep. 2017.
- [4] M. Gomi, T. Kataoka, J. Hayashi, and S. Kakio, "High-coupling leaky surface acoustic waves on LiNbO_3 or LiTaO_3 thin plate bonded to high-velocity substrate," *Jpn. J. Appl. Phys.*, vol. 56, no. 7S1, Jun. 2017, Art. no. 07JD13.
- [5] N. F. Naumenko, "Multilayered structures using thin plates of LiTaO_3 for acoustic wave resonators with high quality factor," *Ultrasonics*, vol. 88, pp. 115–122, Aug. 2018.
- [6] N. F. Naumenko, "High-velocity non-attenuated acoustic waves in $\text{LiTaO}_3/\text{quartz}$ layered substrates for high frequency resonators," *Ultrasonics*, vol. 95, pp. 1–5, May 2019.
- [7] N. F. Naumenko, "Optimization of $\text{LiNbO}_3/\text{quartz}$ substrate for high frequency wideband SAW devices using longitudinal leaky waves," *IEEE Trans. Ultrason., Ferroelectr., Freq. Control*, vol. 67, no. 7, pp. 1485–1491, Jan. 2020.
- [8] N. F. Naumenko, "Advanced substrate material for SAW devices combining LiNbO_3 and langasite," *IEEE Trans. Ultrason., Ferroelectr., Freq. Control*, vol. 67, no. 9, pp. 1909–1915, Sep. 2020.
- [9] N. Naumenko, "Leaky surface acoustic wave with velocity 10 km/s and suppressed leakage in LiNbO_3 plate bonded to sapphire," in *Proc. IEEE Int. Ultrason. Symp. (IUS)*, Sep. 2020, pp. 1–4, doi: 10.1109/IUS46767.2020.9251381.
- [10] A. Tag et al., "Next generation of BAW: The new benchmark for RF acoustic technologies," in *Proc. IEEE Int. Ultrason. Symp. (IUS)*, Venice, Italy, Oct. 2022, pp. 1–4.
- [11] T. Yokoyama, Y. Iwazaki, Y. Onda, T. Nishihara, Y. Sasajima, and M. Ueda, "Highly piezoelectric co-doped AlN thin films for wideband FBAR applications," *IEEE Trans. Ultrason., Ferroelectr., Freq. Control*, vol. 62, no. 6, pp. 1007–1015, Jun. 2015.
- [12] E. Butaud et al., "Innovative smart cut piezo on insulator (POI) substrates for 5G acoustic filters," in *IEDM Tech. Dig.*, Dec. 2020, p. 34, doi: 10.1109/IEDM13553.2020.9372020.
- [13] M. Gorisse et al., "High frequency LiNbO_3 bulk wave resonator," in *Proc. Joint Conf. IEEE Int. Freq. Contr. Sym. Eur. FreqandTime Forum (EFTF/IFC)*, Apr. 2019, pp. 1–2.
- [14] M. Bousquet et al., " LiNbO_3 film bulk acoustic resonator for n79 band," in *Proc. IEEE Int. Ultrason. Symp. (IUS)*, Oct. 2022, pp. 1–5, doi: 10.1109/IUS54386.2022.9957601.
- [15] M. Kadota and T. Ogami, "5.4 GHz Lamb wave resonator on LiNbO_3 thin crystal plate and its application," *Jpn. J. Appl. Phys.*, vol. 50, no. 7S, Jul. 2011, Art. no. 07HD11.
- [16] V. Plessky, S. Yandrapalli, P. J. Turner, L. G. Villanueva, J. Koskela, and R. B. Hammond, "5 GHz laterally-excited bulk-wave resonators (XBARs) based on thin platelets of lithium niobate," *Electron. Lett.*, vol. 55, no. 2, pp. 98–100, Nov. 2018.
- [17] Y. Yang, L. Gao, R. Lu, and S. Gong, "Lateral spurious mode suppression in lithium niobate A_1 resonators," *IEEE Trans. Ultrason., Ferroelectr., Freq. Control*, vol. 68, no. 5, pp. 1930–1937, May 2021, doi: 10.1109/TUFFC.2020.3049084.
- [18] M. Solal et al., "A 4.5 GHz surface excitation solidly mounted micro-acoustic resonator with 20% coupling," in *Proc. IEEE Int. Ultrason. Symp. (IUS)*, Oct. 2022, pp. 1–4.
- [19] S. Yandrapalli, V. Plessky, J. Koskela, V. Yantchev, P. Turner, and L. G. Villanueva, "Analysis of XBAR resonance and higher order spurious modes," in *Proc. IEEE Int. Ultrason. Symp. (IUS)*, Oct. 2019, pp. 185–188.
- [20] S. Yandrapalli, S. E. Kucuk, B. Atakan, V. Plessky, and L. G. Villanueva, "Fabrication and analysis of thin film lithium niobate resonators for 5 GHz frequency and large K_1^2 applications," in *Proc. IEEE 34th Int. Conf. Micro Electro Mech. Syst. (MEMS)*, Jan. 2021, pp. 967–969.
- [21] J. Koulakis, J. Koskela, W. Yang, L. Myers, G. Dyer, and B. Garcia, "XBAR physics and next generation filter design," in *Proc. IEEE Int. Ultrason. Symp. (IUS)*, Sep. 2021, pp. 1–5.
- [22] N. Naumenko, "Laterally excited bulk acoustic resonators (XBARs): Optimization method and application to resonators on LiTaO_3 ," in *IEEE MTT-S Int. Microw. Symp. Dig.*, Jul. 2022, pp. 70–73.
- [23] N. Naumenko, "Optimization method for single-mode performance of laterally excited BAW resonators (XBARs)," in *Proc. IEEE Int. Ultrason. Symp. (IUS)*, Venice, Italy, Oct. 2022, pp. 1–4.
- [24] N. F. Naumenko, "Advanced numerical technique for analysis of surface and bulk acoustic waves in resonators using periodic metal gratings," *J. Appl. Phys.*, vol. 116, no. 10, Sep. 2014, Art. no. 104503.
- [25] N. F. Naumenko, K. B. Yushkov, and V. Y. Molchanov, "Extreme acoustic anisotropy in crystals visualized by diffraction tensor," *Eur. Phys. J. Plus*, vol. 136, no. 1, p. 95, Jan. 2021.
- [26] R. Lu, Y. Yang, S. Link, and S. Gong, " A_1 resonators in 128° Y-cut lithium niobate with electromechanical coupling of 46.4%," *J. Microelectromech. Syst.*, vol. 29, no. 3, pp. 313–319, Jun. 2020.



Natalya F. Naumenko (Member, IEEE) received the M.Sc. and Ph.D. degrees in physics of dielectrics and semiconductors from Moscow Technological University (MISIS), Moscow, Russia, in 1979 and 1984, respectively.

From 1995 to 2011, she was a Consultant in materials for surface acoustic wave (SAW) devices at the companies SAWTEK, Orlando, FL, USA, and TriQuint Semiconductors, Hillsboro, OR, USA. Since 2011, she has been a Consultant and performed research project for different SAW companies: TDK-EPCOS, Munich, Germany; CTR, Villach, Austria; and HUAWEI, Shenzhen, China. She is currently with the Acousto-Optical Research Center, National University of Science and Technology MISIS, Moscow, and the Research Department, Moscow Technical University of Communications and Informatics, Moscow. She is the author of 16 issued U.S. patents and more than 100 publications in SAW material research. Her current research interests include different aspects of acoustic wave propagation in crystals and multilayered structures, and the development of improved simulation tools for the design of SAW and BAW devices, such as resonator SAW filters, delay lines, and wireless SAW sensors.

Dr. Naumenko has been a member of the Technical Program Committee of the IEEE Ultrasonic Symposium since 2011.